Morphology, flow structure, and suspended bed sediment transport at two large braid-bar confluences

Ricardo N. Szupiany,[1] Mario L. Amsler,[1] Daniel R. Parsons,[2] and James L. Best[3]

Received 9 July 2008; revised 6 February 2009; accepted 3 March 2009; published 19 May 2009.

[1] Mid-channel bars and their associated confluences are key morphodynamic nodes within braided rivers, with past studies having investigated the morphodynamics of small natural channels or laboratory models with relatively low width/depth (*W*/*D*) ratios, typically at <10. This paper investigates the morphology, suspended bed sediment distribution, and flow structure at two large braid bar confluences in the Río Paraná (Argentina), wherein *W*/*D* ratios are much higher (approaching 100) than in smaller channels. The results highlight the significant control of the cross-sectional distribution of downstream flow velocity on confluence flow, suspended bed sediment concentration, and morphodynamics and indicate that this factor may become progressively more significant with increasing channel scale and *W*/*D* ratio, particularly when simple discharge (or momentum) ratios between the incoming flows are used to explain the flow dynamics. Additionally, secondary flow cells, often proposed to occupy a large part of the channel width in small river channel confluences, are only identified in relatively small portions of the channel width at these larger spatial scales. Such a restriction seems related to the generative mechanisms of secondary flows at these higher *W*/*D* ratios, which are likely to be dominated by turbulence generated along the mixing layer between the two flows and topographic influences that limit the spatial extent of these effects. This paper highlights the importance of these findings with respect to the flow and sediment dynamics of large channel confluences.

Citation: Szupiany, R. N., M. L. Amsler, D. R. Parsons, and J. L. Best (2009), Morphology, flow structure, and suspended bed sediment transport at two large braid-bar confluences, *Water Resour. Res.*, *45*, W05415, doi:10.1029/2008WR007428.

1. Introduction

[2] Midchannel bars and islands in braided rivers are connected by zones of flow convergence, constriction, expansion and bifurcation, where interactions between the channel morphology and sediment transport are critical in controlling the hydrological and sedimentological behavior of such rivers. A critical region of flow within such morphological units is the confluence hydrodynamic zone (CHZ) [*Rhoads and Kenworthy*, 1998], whose morphology and flow structure have been described extensively in the literature. For example, the position and size of regions of scour and deposition, in relation to both flow structure and sediment transport rates, have been elucidated through field and laboratory research [e.g., *Mosley*, 1975, 1976, 1982; *Ashmore and Parker*, 1983; *Best*, 1986, 1987, 1988; *Boyer et al.*, 2006; *Best and Rhoads*, 2008]. These investigations have documented the existence of several flow features typically found at confluences [*Best*, 1987; *Biron and Lane*, 2008]: (1) a zone of flow stagnation near the upstream junction corner; (2) shear and mixing layers where the two flows combine; (3) zones of separated flow below the downstream junction corner and associated with the avalanche faces of bars at the mouths of each tributary; (4) secondary currents where the flows converge, which are associated with curvature of the flow streamlines, (5) flow acceleration where the two flows converge; and, (6) progressive recovery of the flow downstream from the confluence. The bed morphology of confluences has been found to often reflect these hydrodynamic zones [*Best*, 1986, 1987, 1988; *Rhoads and Kenworthy*, 1995, 1998; *Best and Rhoads*, 2008] with (1) a scour hole that is normally oriented along the region of maximum velocity where both flows begin to converge and mix, and whose orientation often bisects the confluence angle; (2) avalanche faces at the mouth of each tributary, which dip into a central scour hole; (3) sediment deposition within the stagnation zone at the upstream junction corner; and (4) bars formed within the flow separation zone at the downstream junction corner or mid-stream in the post-confluence channel. Previous research has also found that the principal variables controlling the flow structure and channel morphology are (1) the confluence angle and its planform asymmetry [*Mosley*, 1976; *Ashmore and Parker*, 1983; *Best*, 1987, 1988], (2) the flow, or momentum, and sediment discharge ratios between the two confluent channels [*Mosley*, 1976; *Best*, 1987, 1988; *Rhoads*, 1996], and (3) the degree of bed concordance between the two confluent rivers [*Best and Roy*, 1991; *Biron et al.*, 1996a, 1996b]. When the beds of

[1]National Council of Scientific and Technical Researches (CONICET), College of Engineering and Water Sciences, Littoral National University, Santa Fe, Argentina.
[2]School of Earth and Environment, Earth and Biosphere Institute, University of Leeds, Leeds, UK.
[3]Departments of Geology and Geography and Ven Te Chow Hydrosystems Laboratory, University of Illinois, Urbana, Illinois, USA.

0043-1397/09/2008WR007428$09.00

the tributaries are discordant and enter the junction at different elevations, the distortion of the shear layer between the two tributary flows as they combine tends to be the dominant flow feature [*Best and Roy*, 1991; *De Serres et al.*, 1999; *Biron et al.*, 2002], whereas when the two tributaries are concordant, the scour hole position and back-to-back secondary flow cells typically associated with the scour can dominate [*McLelland et al.*, 1996; *Rhoads*, 1996; *Rhoads and Kenworthy*, 1998; *Biron et al.*, 2002]. Understanding the morphodynamic conditions of this region is thus central to enabling further insights into the transfer and distribution of flow and sediment through confluence bar units, and the behavior of the river channel as a whole.

[3] Despite the substantial progress made from previous studies reporting measurements of the characteristics of flow at such sites, the vast majority of this research has concerned relatively small-scale field sites [*Best*, 1988; *McLelland et al.*, 1996; *Rhoads and Sukhodolov*, 2001], detailed measurements in laboratory flumes [*Best*, 1988; *Best and Roy*, 1991; *Biron et al.*, 1993a, 1993b, 2002], or numerical models with boundary conditions based on these small-scale field and laboratory studies [e.g., *Bradbrook et al.*, 2000, 2001]. Exceptions include work detailing the morphology of large junctions [*Klassen and Vermeer*, 1988; *Best and Ashworth*, 1997; *Sambrook Smith et al.*, 2005] and recent work examining flow mixing at large river confluences [*Lane et al.*, 2008; *Parsons et al.*, 2008]. *Parsons et al.* [2008] highlight some of the similarities and differences between the flow and bed morphology of small and large confluences, showing that although many aspects of the gross planform geometry are similar, some differences exist as spatial scale changes. They attribute this both to increasing W/D ratio with channel scale [see *Xu*, 2004], an increase in the role of form roughness and possible differences in the mechanisms generating secondary flows as channel scale increases. However, they also highlight that there is a significant gap in our current understanding, as well as a paucity of data, to address the issue of how concepts from smaller channels relate to processes occurring within much larger rivers, whose channels tend to have much higher W/D ratios [*Xu*, 2004]. Indeed, due mainly to a lack of adequate instrumentation and methodologies adapted to investigations at such large spatial scales, studies of confluence dynamics in large sand-bed rivers have been rare. However, recent developments in technology, especially global positioning systems and acoustic Doppler profiling, have begun to facilitate investigations of the dynamics of large river channels [e.g., *Ashworth et al.*, 2000; *Richardson et al.*, 1996; *Richardson and Thorne*, 1998, 2001; *McLelland et al.*, 1999; *Parsons et al.*, 2007, 2008; *Szupiany et al.*, 2007].

[4] The present paper details the morphology, transport of suspended bed sediment and flow structure, of two asymmetrical bar-confluence units in the Río Paraná, Argentina, where the W/D ratio is very large and typical reach averages approach 100. Both primary and secondary currents, and their relationships with the suspended sand distribution, are considered herein. The results expand the present database on confluence dynamics to large sand-bed river channels and provide an opportunity to begin to identify and analyze the similarities and differences between confluences of different spatial scales. The paper begins to identify how process differences are manifested, and alter the mechanisms generating secondary flows, as channel scale increases and discusses the implications of this for the dynamics of channel confluences.

2. Study Sites, Field Procedures, and Methods

2.1. Study Sites

[5] The Río Paraná is one of the largest rivers in the World [*Schumm and Winkley*, 1994], with a drainage basin of 2.3×10^6 km^2 that includes parts of Brazil, Bolivia, Paraguay and Argentina. Downstream of the major confluence with the Río Paraguay (Figure 1), the mean annual discharge of the Río Paraná is 19,500 m^3 s^{-1}, and the water surface slope is in the order of 10^{-5}. The channel bed is composed largely of fine and medium sand [*Drago and Amsler*, 1998], and the channel planform pattern has been classified as braided with a meandering thalweg [e.g., *Ramonell et al.*, 2002]. In planform, the river has a succession of wider and narrower nodal sections, with mean channel widths and depths ranging between 600 to 2,500 meters and 5 to 16 meters, respectively.

[6] The study area detailed herein is located in the lower reaches of the Río Paraná near the cities of San Martín (A) and Rosario (B) (Figure 1). The two sites investigated comprise large, asymmetrical, bar-confluences, with the San Martín site (Site A) being surveyed on 13 June 2006 and the Rosario site (Site B) being surveyed on 7 June 2006 (Figure 1). On these dates, the total flow discharge was approximately 14,500 m^3 s^{-1} (Table 1).

2.2. Bathymetric and Three-Dimensional Flow Mapping

[7] At these two bar-confluences, the river bed morphology was surveyed using a Raytheon single beam echo sounder, coupled to a differential global positioning system (DGPS), which was deployed on a small survey vessel. The DGPS provided horizontal positions to an accuracy of ±1 m at approximately 1 Hz. Morphological measurements were made along a series of cross sections through the bar confluences, with each line being separated by approximately 100 meters. The point x, y, z morphological data were interpolated using standard kriging methods onto a regular grid to create bathymetric maps of the two bar-confluence regions. Once the bathymetry had been obtained, the three-dimensional flow velocity was measured with a 1000 kHz Sontek acoustic Doppler profiler (aDp). At each of the sites, flow measurements were made at 5 individual cross sections that were chosen to provide details on the incoming flow fields and postconfluence flow structure (Figure 1). Since the aDp was deployed from a moving vessel, it was linked to the DGPS to provide both position and boat velocity. The bottom tracking function of the aDp was not used for boat motion due to the measurement errors that bed load transport can introduce into the results obtained [*Kostaschuk et al.*, 2005]. The boat velocity and track position of the survey lines were monitored online by the helmsman and held as constant as possible during surveying, with a steady boat velocity of $\sim$1.5 m s^{-1} [see *Szupiany et al.*, 2007, for details]. The aDp used herein has 3 divergent monostatic transducers (beams), oriented at 25° to the vertical and spaced at 120° from each other [*Sontek*,

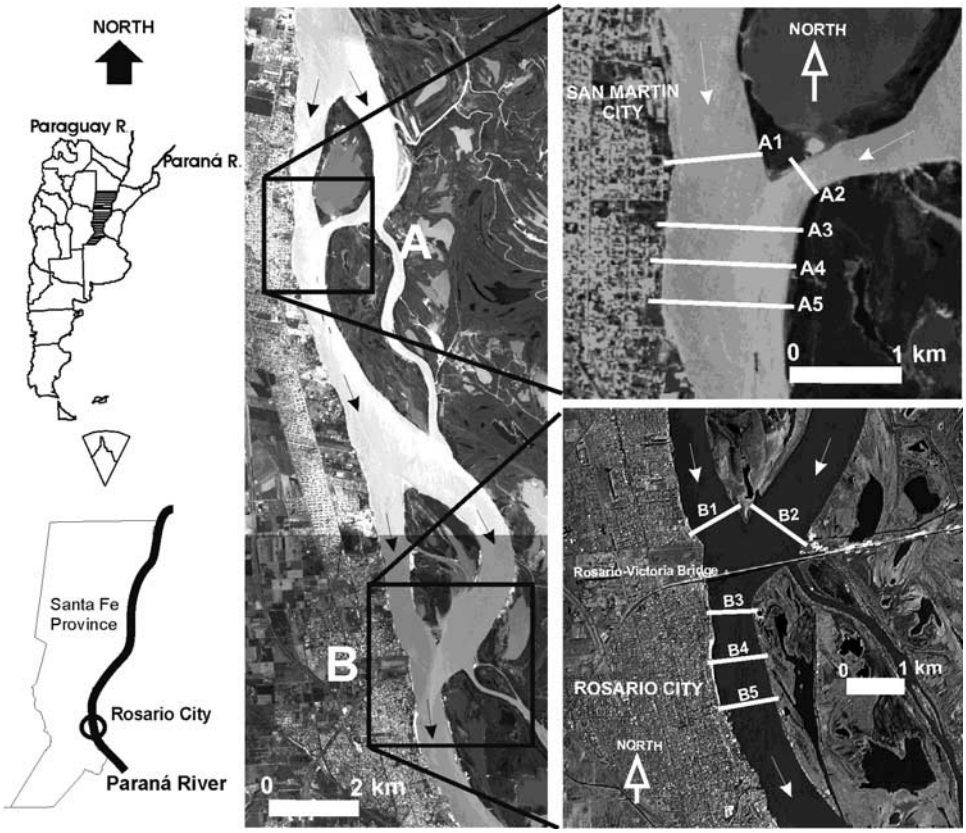

Figure 1. Location of the study sites and measured cross sections within the two confluences.

2000]. The cell size (*CS*) and the averaging interval (*AI*), or ensemble, used herein were 0.75 meters and 10 seconds, respectively. In moving vessel measurements, the velocity values represent the flow at a position halfway between two ensembles, since during the *AI* the boat moves at a certain speed (i.e. the width of the measured water column will depend on the *AI* and the boat speed). Due to the beam separation, the water velocities are also spatially-averaged in a cone-shaped volume, the diameter of which expands according to $0.93d$, where d is the distance below the aDp transducer. These factors thus imply an assumption of temporal and spatial flow homogeneity in the measured volumes, which become particularly large at greater flow depths. This assumption may be valid depending on the flow characteristics. Considering an *AI* of 10 seconds and a boat speed of 1.5 m s^{-1} (of the order of the flow velocity), the measured velocity would represent the flow conditions of an average volume that is 15 m in length, $0.93d$ in width and 0.75 m in height. In the Rio Paraná, with channel widths ranging between ~600 m to 2,500 m, this assumption of flow homogeneity would thus be properly satisfied at this scale. However, the spatial and temporal averaging of the acoustic profiles obtained from a single transect with a moving vessel yielded a scatter in the measured velocity values, which although adequate for discharge measurements, was deemed unacceptable for analysis of the detailed flow structure. Therefore in order to obtain representative values of the time-averaged three-dimensional velocities at each cross section, a series of 5 repeat transect lines were collected and subsequently averaged. *Szupiany et al.* [2007] detail this averaging process in full and show how this provides confidence in the repeatability of the section results and the subsequent identification of three-dimensional flow patterns.

2.3. Shear Stress Determination

[8] The average velocity profiles obtained with the aDp mobile vessel measurements were used to estimate the total bed shear velocity values, U_*, by applying the law-of-the-wall in the manner suggested by *Kostaschuk et al.* [2004] and following the methodology proposed by *Szupiany et al.*

Table 1. Main Geometric and Hydraulic Characteristics of Confluences A and B

	A			B		
Characteristic Parameters	A2	A1	A3	B2	B1	B3
Mean flow velocity (m s^{-1})	0.81	1.08	1.03	0.81	0.94	1.0
Maximum flow velocity (m s^{-1})	1.25	1.63	1.73	1.09	1.14	1.26
Width (m)	310	700	1000	565	935	900
Discharge (m^3 s^{-1})	2420	12250	14670	4800	9538	14338
Mean depth (m)	7.95	16.2	14.3	10.4	10.6	10.6
Maximum depth (m)	12.4	25.6	18	13.9	18	23.4
Junction angle (degrees)		77			70	
α_L[a]		77			70	
α_R[a]		0			0	
Flow momentum ratio, M[b]		0.15			0.43	
Discharge ratio		0.2			0.5	

[a] α_L and α_R are the angle of deviation between the left and right branches relative to the downstream channel.

[b] $M = (\rho Q_L V_L)/(\rho Q_R V_R)$, wherein ρ = water density (kg m^{-3}), Q = total discharge (m^3 s^{-1}), V = cross-section average velocity (m s^{-1}), and the subscripts L and R denote the left and right branches, respectively.

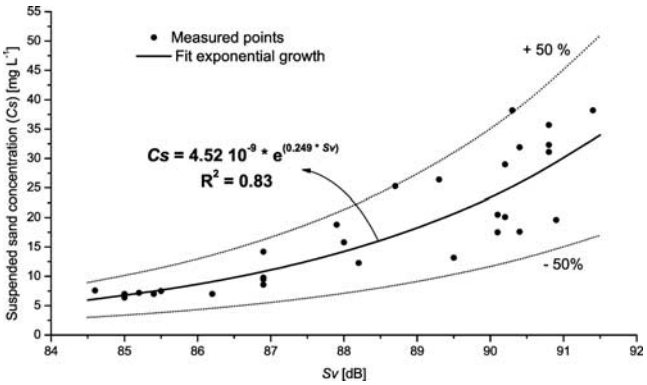

Figure 2. Relationship between corrected aDp backscatter (*Sv*) and measured suspended sand concentrations (*Cs*).

[2007], where values of U_* were determined from linear regressions of the form:

$$v = a(\ln z) + b \tag{1}$$

so that

$$U_* = \kappa a \tag{2}$$

where v = flow velocity, z = height above bed, κ is the von Karman constant ($\sim$0.4), a is the regression slope coefficient, and b is the regression intercept coefficient (roughness zero height). Regression slopes (a) determined for the data sets ranged from 0.04 to 0.23, and the zero heights estimated from the regression equations were realistic for a large sand bed river, with values varying in the range 0.3 to 1.0 m. Previous work in same river [*Amsler and Schreider*, 1999] has determined zero heights of 0.65 m, due to the influence of dunes, providing confidence in the regression equation estimates applied herein.

[9] The bed shear stress (τ) was then computed from

$$\tau = \rho U_*^2. \tag{3}$$

This relatively simplistic approach allows for a quasi-quantitative analysis of the relative distribution of shear stress through the confluence zones and provides additional process understanding.

2.4. Suspended Bed Sediment Mapping

[10] There is increasing recognition that acoustic Doppler technology can be used to provide quantitative information on suspended sediment concentrations [*Creed et al.*, 2001; *Filizola and Guyot*, 2004; *Kostaschuk et al.*, 2005; *Sontek*, 1997] through analysis of the intensity of the acoustic backscatter strength. This intensity will be a function of both the equipment characteristics (frequency, transmitted power, measured volume range, received sensitivity) and the flow conditions (concentration and size of sediment particles, amount of organic matter, dissolved solids and air bubbles, [*Sontek*, 1997]). Therefore for a given instrument, a constant sediment type and grain size distribution, and in the absence of air bubbles and particulate organic matter, the signal strength will have a simple relation with the sediment concentration.

[11] The backscatter intensity recorded by the instrument may be computed by the simplified sonar equation:

$$EL = SL + 10^* \log_{10}(PL) - 20^* \log_{10}(R) - 2^* \alpha_s {}^* R + Sv + RS, \tag{4}$$

where EL is the signal intensity as reported by the instrument; PL, SL and RS are parameters whose values depend only upon the instrument characteristics; R is the distance between the transducer and the measured volume; α_s is the sound absorption coefficient, and Sv is the volume scattering strength. Equation (4) suggests that direct comparisons between different types of equipment would not be possible since each one would require its own calibration process to set the values of specific parameters (SL, PL, and RS). Thus it is necessary to quantify the suspended sediment for a specific instrument with a relationship obtained directly between concentrations measured *in situ* with standard direct sampling methods, and the corresponding volume scattering strength (also called the corrected backscatter intensity). Estimation of the volume scattering strength (Sv) requires that the signal intensities reported by the instrument should be corrected (see equation 1) due to the decay effects of the geometric spreading ($-20\log_{10}$R) and absorption (-2 * α_S * R). The first term is simply a geometric term due to the cone shape of the acoustic beams, and the second term is due to molecular transfer of acoustic energy to heat. There is an additional term due to spreading and absorption of acoustic energy by the particles in the water, but at low sediment concentrations this term is small and can be ignored [*Sontek*, 1997]. The procedure also requires negligible quantities of organic matter and a specific cell size since this setting affects the length of the acoustic pulse, PL, with a longer aDp pulse setting resulting in larger signal strengths. Finally, the backscatter is sensitive to the suspended particle size distributions for a given concentration. The 1000 kHz Sontek aDp used in the present study has its largest sensitivity to particles with a radius (pr) of 235 μm. Additionally, individual non-interacting particles with $pr \lesssim$ 12 μm would not be detected, with the relative sensitivity being less for particles smaller than $\sim$50 μm. This characteristic of the system is particularly important in a sand-bed river like the Río Paraná, since in such rivers the suspended load is composed of the washload (normally silts and clays) and suspended bed material (normally sands). Thus in the case of this aDp, the suspended sand concentration would dominate the backscatter signal measured since the washload in the Río Paraná is composed largely of particles $\lesssim$40 μm in radius and normally with concentrations smaller than 400–500 mg L^{-1} along its lower reach [*Drago and Amsler*, 1988]. These amounts of fine sediment are unlikely to increase absorption of the acoustic signal [*Sontek*, 1997] and thus the backscatter can be used to estimate the amount of suspended sand-grade material.

[12] Based on the above rationale, a good relationship can be obtained between the corrected backscatter signal of the aDp and the directly measured suspended sand concentrations (Figure 2). To derive such a relationship for the field site, depth-integrated direct samples were obtained at 29 separate vertical profiles. These were obtained at a range of

locations and depths across the Río Paraná channels in order to obtain a wide distribution of flow conditions and concentrations. Simultaneous to the direct sampling, fixed-vessel measurements were made with the aDp. The aDp acoustic backscatter was sampled for over 400 seconds at each vertical location, using a vertical cell size of 0.75 m and an averaging interval of 10 s. The depth-integrated samples identified that concentrations of suspended sand (*Cs*), washload (*Cw*), and dissolved solids (*Cds*) ranged between 6.2–38.2 mg L^{-1}, 85.2–370 mg L^{-1}, and 56.4–92 mg L^{-1} respectively. Although the results indicate that the washload concentrations are higher than suspended sand concentrations, as the washload particle sizes are relatively small then their influence on the aDp backscatter is considerably lower than the suspended sand. The concentration of dissolved solids was used to estimate the sound absorption coefficient, α_S, that is required to compute the corrected backscatter intensities (equation (4)). The backscatter intensities of each cell for a given vertical were averaged in order to correlate these with the corresponding depth-integrated concentration measured at that point. The correlation between suspended sand concentration and the corrected backscatter intensity presents a good agreement, reflected by a regression coefficient (R^2) of 0.83 (Figure 2). The relationship between the backscatter intensities versus 10log(*Cs*) is linear with a slope close to 1:1.

[13] Using this relationship, it was thus possible to estimate the average suspended sand concentrations at each cross-section through both confluences. The product of the derived point concentrations and corresponding velocities given by the aDp was then used to determine the total suspended sand transport flux across each cell, *CS,* and the suspended sediment transport through the entire section, *Gss*. The transport of sand through portions of the sections that were not measured by the aDp (i.e. the top aDp blanking distance (0.6 m), the ~10 % of depth nearest the bed and at the ends of the sections), were estimated using simple linear interpolations to the boundaries.

2.5. Identification of Secondary Currents in Large Rivers: Definitions and Methods

[14] The velocity vectors at confluences tend to cross obliquely relative to any applied cross-sectional reference system, and the magnitude of any cross-stream component of velocity may thus be dominated by skewed flow through the section, therefore potentially obscuring identification of any underlying coherent secondary circulation within the flow field. Therefore a reliable procedure must be adopted to elucidate secondary velocities from the velocity measurements. The correct and robust definition of secondary currents within river channels has been a source of recent debate [*Lane et al.*, 1999, 2000; *Rhoads and Kenworthy*, 1999], and *Lane et al.* [2000] summarize the calculation methods and classification of secondary flows into 4 definitions: (1) the centerline definition; (2) the Rozovskii definition; (3) the zero net cross-stream discharge definition; and (4) the discharge continuity definition.

[15] In the Río Paraná, with very large average channel widths (see above), several constraints exist on the methods of data collection and rotation of secondary current vectors, including significant transverse variations in the main flow direction that can often complicate identification of the primary flow direction and thus definition of a robust frame of reference. Moreover, the location of a given reference section is particularly difficult to determine at confluences and bifurcations, since the primary flow changes its curvature permanently and in opposite directions at both sides of the confluence mixing layer or at the bifurcation flow division line. These constraints result in the centerline definition and methods that define only one secondary plane across an entire section (i.e. the discharge continuity and the zero net cross-stream discharge procedures) for rotation of secondary velocities often being problematic to apply, particularly given the greater possibility of flow wandering, division and combination, and the requirement of closely spaced cross-sections. The present paper has thus used the Rozovskii definition, as this allows any rotation to be based upon individual verticals, rather than rotation of the whole section. This method essentially identifies the primary velocity direction for each profile as the depth-integrated flow vector, and the secondary currents are then obtained by the differences from this average vector within the profile. This procedure effectively identifies individual secondary planes at each vertical profile across a given section, thus permitting identification of variations in the primary flow direction within a section, without distorting the secondary flow results.

[16] Past studies have elucidated two main features of helical motions: (1) the direction of the primary velocity vectors changes consistently, with maximum deviation angles near the water surface and near the bed and (2) this pattern is maintained across many verticals [*Rhoads and Kenworthy*, 1995]. The Rozovskii method captures these features fairly well and displays the secondary component field as derived from the divergence of the primary vectors between surface and bed.

[17] In the Rosovskii method, the primary (v_P) and secondary (v_S) components of each point velocity at a vertical are computed from:

$$v_P = v\cos(\theta - \alpha) \tag{5}$$

$$v_S = v\sin(\theta - \alpha) \tag{6}$$

$$v = \sqrt{v_N^2 + v_E^2}, \tag{7}$$

where v is the point velocity vector, θ is the orientation of v with respect to north, v_N, v_E are the northerly and easterly components of the point velocity vector, and α is orientation with respect to north for the depth-averaged velocity vector. Following *Rhoads and Kenworthy* [1998], α was fixed from the direction of the depth-averaged velocity vector defined by integrating v_N and v_E separately over the entire flow depth for each vertical profile.

3. Results

3.1. General Hydraulic and Morphologic Characteristics

[18] The gross geometric and hydraulic conditions of confluences A and B during the surveys are summarized in Table 1. The junction angle at each of the sites was measured using the average thalweg path along both

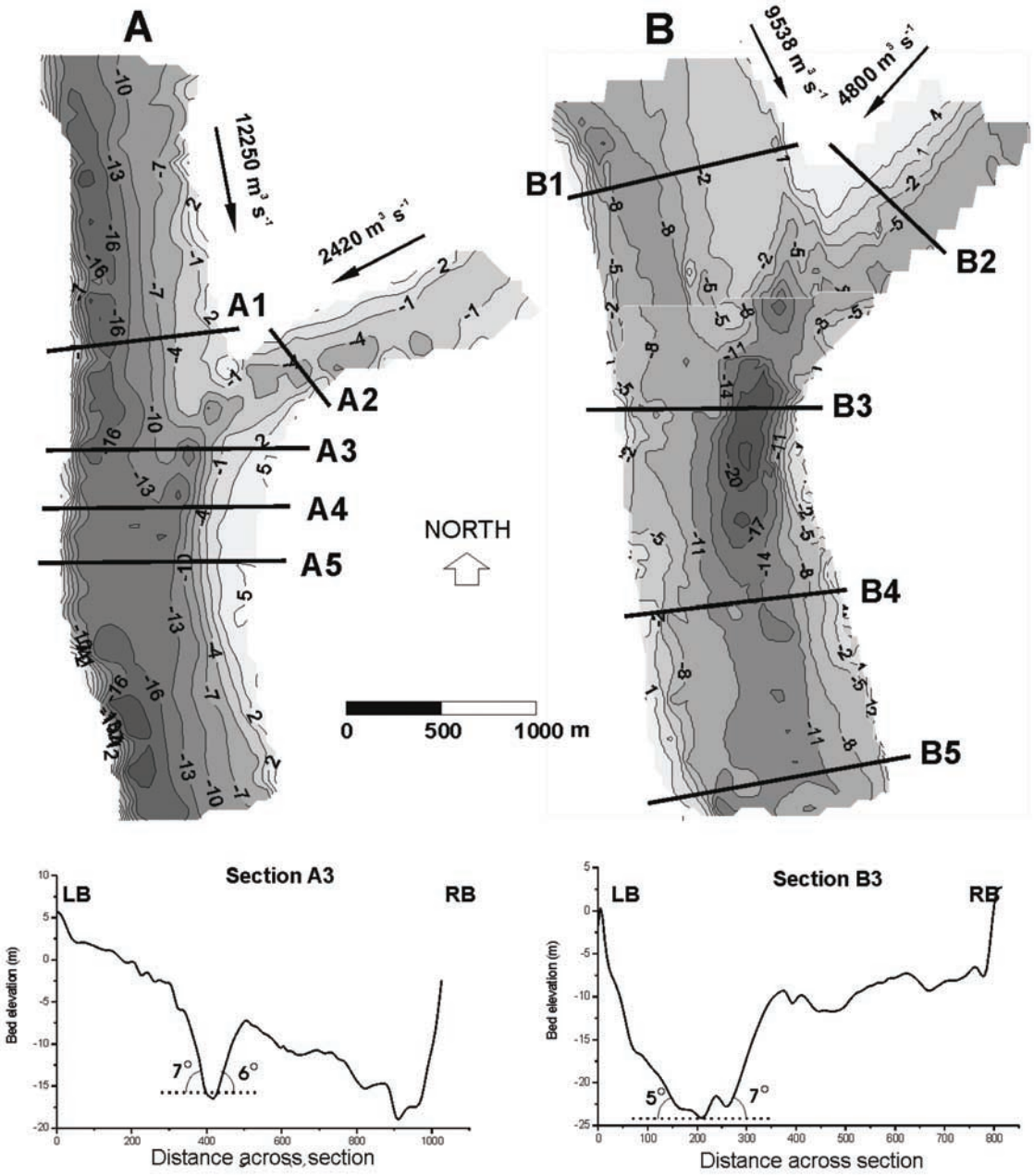

Figure 3. Bed contour maps of confluences A and B (depths refer to the 0 m level at the Rosario Port gauge). Survey date: 13 June 2006 (confluence A) and 7 June 2006 (confluence B). Water levels: 2.74 m and 2.25 m, respectively. Note: cross-section panels are viewed looking downstream with left bank on the left-hand side.

branches, with the angles being very similar at 77° and 70° in confluences A and B respectively. River stage was also approximately equal during the two surveys, with the stage records at Rosario Port being 2.3 m on 7 June and 2.7 m on 13 June. At both sites, the right branch channel dominates in its flow discharge but, due to differences in channel configuration, the discharge and momentum ratios are different at confluences A and B (see Table 1).

[19] Maps of the channel bed topography (Figure 3) show that at confluence B although the incoming channels are of a similar depth with no distinct discordance in bed elevation, a deep scour is present within the confluence at section B3. The scour is located toward the left bank, where the two flows combine, extends to a depth of approximately 23 m (two to three times the pre-confluence average channel depths) and is around ~1000 m in length. At confluence A, a pronounced discordance in bed height does exist between the confluent channels, with the left channel being much shallower (mean depth ~8 m) than the right channel (mean depth ~16 m). The junction scour at confluence A is not as well defined as at confluence B, and comprises a small central scour area approximately 15 m deep immediately downstream from where the flows initially combine, and this extends into a deeper, larger scour that is a continuation of the pre-confluence right channel thalweg. Such bed discordance, and in particular the slopes of the bed

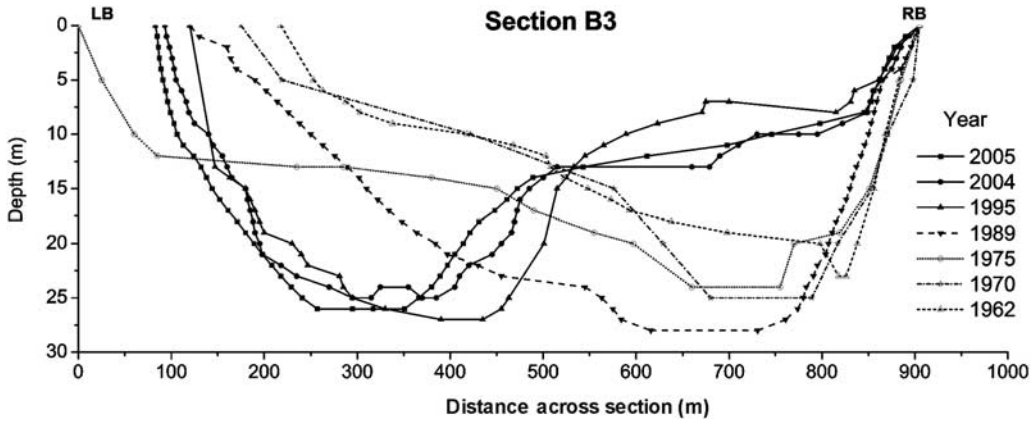

Figure 4. Morphological changes at section B3 (confluence B) in the period 1962–2005. Section is viewed looking downstream with left bank on the left-hand side.

at the mouth of the tributaries, has significantly different characteristics compared with several smaller confluences [*Parsons et al.*, 2008]. At large sand-bed river confluences, such as those reported herein and in some previous research [*Best and Ashworth*, 1997], the slopes of the bed dipping into the scour tend to be small, often lower than ~3 degrees in longitudinal profiles along the scour hole, and ~7 degrees in profiles transverse across the scour hole (Figure 3). Studies of laboratory confluences with both concordant and discordant beds frequently report much higher slope angles, which are often an order of magnitude larger than that reported herein [e.g., *Best*, 1988; *Biron et al.*, 1993a, 1993b, 2002; *McLelland et al.*, 1996; *Rhoads*, 1996], and high enough to yield flow separation at the avalanche faces of the tributary mouth bars [*Best*, 1988; *McLelland et al.*, 1996].

[20] A large bar is present below the downstream junction corner at confluence A, in an identical position to bars formed in regions of flow separation at smaller junctions [e.g., *Best*, 1988; *Reid et al.*, 1989; *Rhoads and Kenworthy*, 1995; *Best and Rhoads*, 2008], although at confluence B such a bar is far less pronounced. Reasons for the difference in the nature of the bed morphology at the two sites appear related to the relative positions of the scour and the rapidity of flow deflection as the flows combine. The influence of the longer-term migration of the channels could also have an influence on the observed differences in bed morphology.

Table 2. Percentages of the Total River Discharge Flowing in Both Confluent Channels at Confluence B During the Last 44 Years

Year	Discharge (%)		Discharge Ratio (Q_L/Q_R)
	Left Branch	Right Branch	
1962[a]	81	19	4.3
1970[a]	78	22	3.5
1979[a]	71	29	2.5
1989[a]	65	35	1.9
1993[b]	50	50	1
2004[c]	37	63	0.6
2006[c]	33	67	0.5

[a][*FCEIA-UNR*, 1990; *SERMAN y Asoc. S.A.*, 1998].
[b][*SERMAN and Asociados S.A.*, 1998].
[c]Present measurements.

The current bed morphology of confluence B can be placed into a broader historical context using past cross sections taken at section B3 (Figure 4) over the period 1962–2005 together with allied discharge records. *FICH* [2006] related the morphological variations at confluence B over this period to (1) the response of the river to medium-term changes in its effective discharge, and (2) total sediment transport, both of which interact within the inherited imposed regional slope. *FICH* [2006] report that the left branch began to lose its dominant role at confluence B during the 1960s, as the right branch progressively increased its size and discharge contribution. Since this time, the channel discharges have adjusted, as clearly shown in Table 2 where temporal records of the percentage of the total flow discharge passing through each branch are given. The geometrical variations in both branches through time, as shown by their mean widths (Table 3), illustrate that the width of the left channel has declined concurrent with the reduction in its flow discharge. The morphological consequences of these upstream channel changes on the position of the scour hole within the immediate cross-section downstream of flow combination (section B3) are shown in Figure 4. It is apparent that there has been a rapid displacement of the scour hole from the right to the left bank since the 1960s until the present survey. Such migration of the scour hole appears intricately linked to evolution of the left and right branches, with the position of maximum depth gradually moving from the right bank to midchannel from 1969 to 1989 when the discharge ratio, Q_L/Q_R, was greater than 1, and then progressively nearer to the left bank when Q_L/Q_R became less than 1. This alteration in Q_L/Q_R has since prevented sedimentation in this region and promoted

Table 3. Evolution of the Río Paraná for Both Confluent Channels at Confluence B, 1954–2004

Year	Mean Width Right Branch (m)	Mean Width Left Branch (m)	Mean Width (m)
1954	No central island		2722
1976	812	1690	2502
1980	891	1595	2486
1987	800	1163	1963
1993	831	1162	1993
2004	880	998	1878

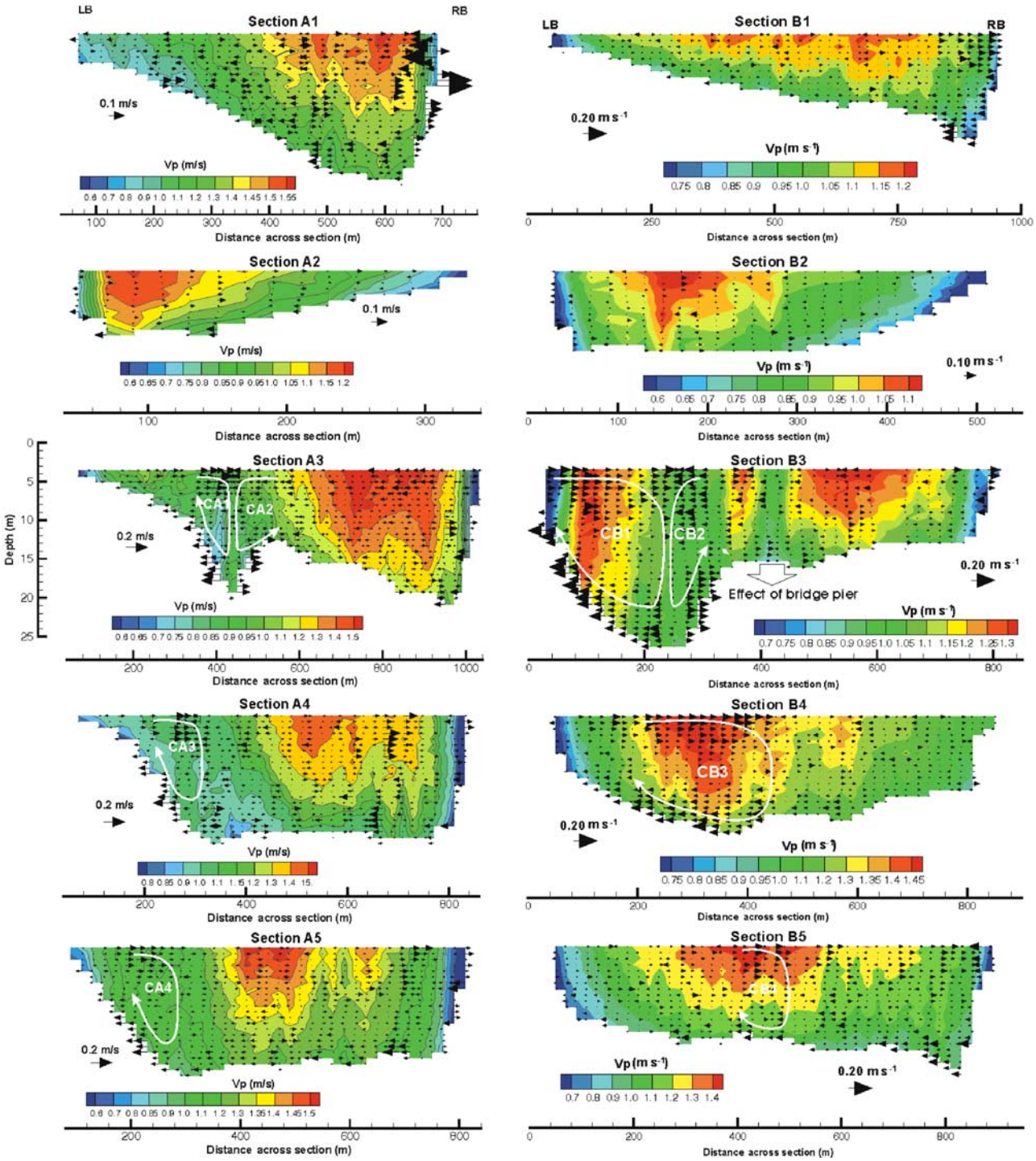

Figure 5. Primary and transverse velocity fields in the surveyed sections at confluences A and B. Sections are viewed looking downstream with left bank on the left-hand side. Note: primary flow is into the page for all sections and the contour range and reference vectors change between plots to aid visualization.

erosion of the left bank, perhaps explaining the lack of a large bar at this location. These movements of the scour, in response to the upstream influence of the two incoming flows, highlight the need for future investigations to link confluence dynamics to the evolution of the upstream channel morphologies and dynamics of any diffluence bar unit.

3.2. Primary Velocity Fields

[21] Figure 5 shows the primary (v_P) and secondary (v_S) components of velocity at the 5 cross-sections at confluences A and B (A1 to A5 at A, and B1 to B5 at B). In both confluences, the first two sections were located upstream of the junction within the confluent channels (A1 and A2 in A, and B1 and B2 in B). The third sections, A3 and B3, were

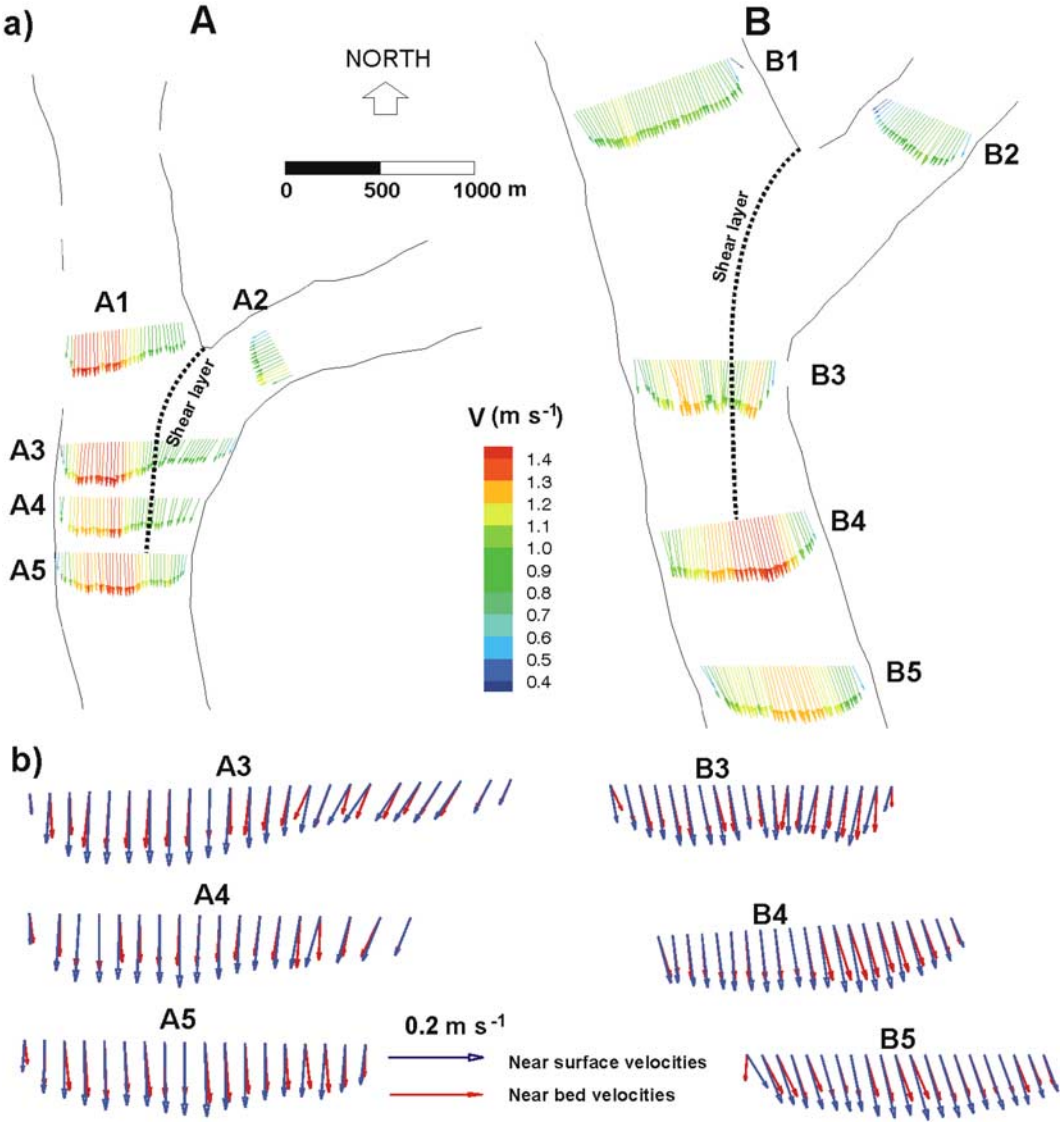

Figure 6. (a) Distribution of vertically-averaged flow velocities through both confluences. (b) Distribution of near-surface and near-bed velocities at the three post-confluent sections at each confluence.

positioned such that they included the maximum depth of the scour hole, while the fourth and fifth sections were located downstream to investigate the structure of flow in the postconfluence channel (Figure 1).

[22] Within both cross-sections across the maximum scour depth, the two cores of maximum primary velocity from the upstream branches remain distinct (A3 and B3, Figure 5), with a zone of lower primary velocity existing within the central area as the flows combine. At confluence B, between 400 to 450 m across section B3, there is an area of slower flow that is interpreted as due to the effect of one of the central piers of the Rosario-Victoria Bridge located just upstream (see Figure 1). This effect dampens rapidly since, in section B4, it is no longer discernable. Nevertheless, the location of the cores of primary velocity in the confluent channels, and in particular their position within the dominant branch channel (the right branch in both cases), appears to exert an important control on the structure of flow as the flows combine. This influence extends to the behavior of the incoming flow from the smaller branch channel. In confluence A, the principal flow in the main branch channel is positioned between the center of the channel and the right bank (section A1), and remains close to the right bank within sections A3 and A4. In confluence B, the main flow in the dominant branch channel is more uniformly distributed across channel (section B1) and maintains that distribution downstream through the main confluence zone.

[23] These distributions are depicted in planform maps of velocity vectors (Figures 6a and 6b) where the vertically averaged flow velocities are plotted for both confluences. A distinct difference is observed when comparing the cross-sectional velocity distribution at sections A3 and B3. In confluence A, the left pre-confluence channel is ~310 m wide with a cross-sectional area of 2761 m^2. At section A3, the discharge supplied by this left branch flows within a width of ~400 m and an area of 3245 m^2, extending between the true left bank and the region of slow primary velocities where the flows combine, i.e. the shear/mixing layer. However, in confluence B the discharge of the pre-

confluence left branch flows though an area of 6170 m^2 with a width of ~560 m and after the confluence this flow is constricted across a smaller width (260 m), with a cross-sectional area of 5350 m^2. This constriction in the downstream direction in confluence B results in flow acceleration between the mixing interface and the left bank at section B3 and promotes erosion of the left bank as observed in Figures 3 and 4. At confluence A, however, despite the lower momentum ratio (Table 1), flow from the left branch channel is not constricted and accelerated as much as the flows combine, permitting the formation of a larger region of low velocity near the bank, possibly with flow separation at the downstream junction corner, and this may explain the larger region of sedimentation within this region. The core of primary velocity in the right branch channel at section A1 is also displaced toward the right bank as far downstream as section A3, and does not produce a large acceleration of flow when mixing with the incoming discharge from the left channel at section A2. Such interactions between the combining flows and lack of large flow acceleration may also explain the existence of a smaller scour hole at confluence A than at confluence B. It is also noticeable that at both confluences there are no upstream-directed mean velocity vectors in the region downstream of the lower junction corner, whereas this location is often characterized by flow separation at smaller junctions [*Best*, 1987; *Rhoads and Kenworthy*, 1998]. The lack of flow separation detected in this region is perhaps a result of (1) the zones being disproportionally small that they avoided detection at the section locations, (2) the rounded junction corners, or (3) the fact that sedimentation within this region creates topographically-steered flows that lead to the cessation of large-scale flow separation, as has also been documented in rectangular channels [*Best*, 1986, 1988].

[24] Downstream recovery of flow at confluence B is relatively rapid, with only one core of primary velocity discernable at sections B4 and B5 (Figure 5), and whose intensity declines downstream as the region of scour becomes shallower. However, at confluence A the two cores of different magnitude velocity are still discernable at both sections A4 and A5 (Figures 5 and 6). This could possibly be due to (1) the role of the greater width constriction at confluence B in accelerating the flow and hastening flow recovery; and/or (2) sections A4 and A5 are relatively closer to the junction and are fewer multiples of channel width downstream as compared to confluence B.

3.3. Transverse and Vertical Velocity Fields and Location of the Mixing Interface

[25] In the central portions of both confluences (sections A3 and B3), two counter-rotating surface-convergent secondary cells (CA1 and CA2 at section A3 and CB1 and CB2 at section B3, Figure 5) are visible across the main scour holes where the two flows converge. These cells have consistent differences in the direction of the near-bed and near-surface transverse velocity vectors (Figure 6), possess velocities that are consistently higher than the measurement errors produced by the aDp [see *Szupiany et al.*, 2007], and are coherent across a portion of the channel width. The limited extent of the coherence in the transverse velocity fields is also shown in the patterns of vertical velocity across the sections (Figure 7), which reveal limited regions of upwelling and downwelling that are located around the mixing layer at the center of the junction and across a small portion of the point bar upstream of Section A1. Although in both confluences the vertical velocities are of relatively low magnitude (Figure 7), they are obtained by transect averaging [*Szupiany et al.*, 2007] and thus significant vertical velocity patterns are present, particularly in the zones close to the mixing/shear interface. These patterns in vertical velocity are used to aid delineation of the extent of the secondary flow cells (Figure 5, Table 4), and improved interpretations of the three-dimensional flow field. Although closer to the precision possible with the aDp, it is also noticeable that the vertical velocities define narrower bands of upwelling and downwelling at other parts of the cross sections (e.g., A5 and B5, Figure 7). This may be linked to the role of form roughness in promoting topographic forcing of flow [*Parsons et al.*, 2007] or deepening though these sections as the flows recover in the post-confluence channel.

[26] The main properties of these secondary flow cells (given in Table 4) show their size is limited with respect to the channel width and that they have relatively weak intensities that represent only a small proportion of the resultant velocity components. The extent of the coherence in the secondary flow cells and the main cores of downstream velocity at each confluence correspond well with both the position of the mixing interface, at ~440 m at section A3 and ~250 m at section B3, and with the areas of maximum depth at each of these sections. Moreover, in both confluences, the secondary flow cells are of a similar spatial extent, flow intensity and pattern, with the cells being larger and more intense toward the left side of the sections A3 and B3 in particular. Nevertheless, given the widths of the channels, the spatial extent of these secondary cells is only limited to a small area of the channel, normally covering less than ~20 % of the channel width, that encompasses the mixing/shear region between the convergent flows near the confluence center. These zones in both confluences are thus characterized by downwelling over the center of the scours and fluid upwelling relatively close to the mixing/shear layer (Figure 7). A second zone of downwelling is also present in section B3 close to the edge of the left bank side of the main scour, perhaps limiting the extent of the junction center secondary cell (CB2, Figure 5). These patterns of vertical velocity (Figure 7) also support the presence of width-restricted, more complex, secondary cells through these larger confluences (Figures 5 and 6), with turbulence across the mixing interface and through the scour appearing to play a crucial role in generating the identified secondary flow cells [*Best and Roy*, 1991; *Lane et al.*, 2000].

[27] Further downstream, at sections A4 and B4, the secondary cells on the left side of the channels (labeled CA3 and CB3, Figure 5), which are present upstream at sections A3 and B3 respectively, maintain some of their coherence, being approximately the same width in section A4 as in section A3 (CA3 is ~90 m) and slightly larger in B4 compared to B3, with the cell width of CB3 increasing to ~220 m. However, the magnitude of the secondary velocities tends to decline in the downstream direction. This decline is particularly notable in the vertical velocities between sections 3 and 4 at both confluences (Figure 7) and when comparing the lateral velocities between sections A4 and A5 (CA3 and CA4) in confluence A and B4 and B5 in confluence B. Indeed, by section B5, the

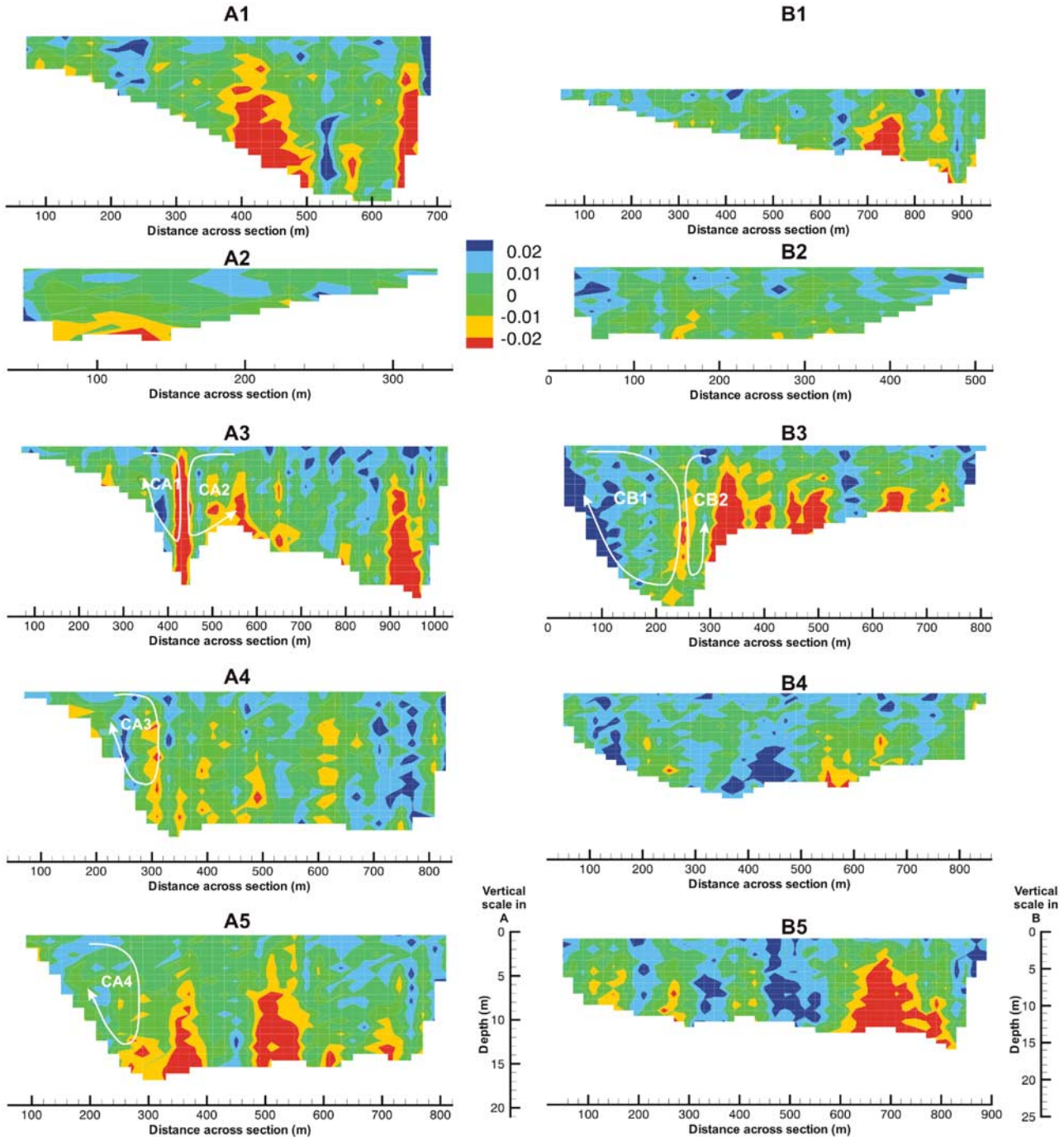

Figure 7. Vertical (V*up*) velocity fields in the surveyed sections at confluences A and B, with positive and negative values denoting flow away from and toward the bed, respectively. Sections are viewed looking downstream with left bank on the left-hand side. The secondary flow cells identified in Figure 5 are shown for comparison. Note: primary flow is into the page for all sections.

strength of the cell (labeled CB4) has declined significantly and is relatively small and weak. The relative distance from the upstream junction corner to section B5 in confluence B is further downstream than section A5 in confluence A ($1W_A$ separating A3 from A5 and $1.8W_B$ separating B3 from B5, where W_A and W_B are the mean widths of the post-confluence channels in confluences A and B respectively), which perhaps explains some of the difference in the dissipation of these secondary flow cells. However, at both confluences the right-hand secondary cells lose their coherence much more rapidly than the secondary cells on the left of the channel and become difficult to determine in both sections A4 and B4.

[28] Analysis of the total discharge passing through various portions of the channel width provides another mechanism to explain the limited spatial extent of the secondary flow cells and the apparent rapid reduction in secondary flow intensity downstream of both confluences.

Table 4. Main Parameters of Transverse Velocities of the Secondary Flow Cells Measured at the Confluences

	Confluence A				Confluence B			
	A3		A4	A5	B3		B4	B5
Section Secondary Cell	*CA1*	*CA2*	*CA3*	*CA4*	*CB1*	*CB2*	*CB3*	*CB4*
Width, A_C (m)	80	70	90	80	220	40	220	80
Relative width (A_C/A_T)	0.08	0.07	0.08	0.10	0.23	0.06	0.23	0.08
Mean transverse velocity (m s^{-1})	0.04	0.04	0.05	0.030	0.04	0.05	0.040	0.030
Maximum transverse velocity (m s^{-1})	0.16	0.5	0.13	0.110	0.16	0.12	0.130	0.080
Relative transverse velocity ($\bar{v}_S/\bar{v}_P$)	0.04	0.04	0.047	0.028	0.04	0.05	0.035	0.029

In confluence B, at sections B4 and B5, nearly 60% of the total fluid flux flows between the true left bank and the right borders of cells CB3 and CB4, respectively, and this flux is much larger than the discharge supplied by the left branch to the confluence hydrodynamic zone (which supplies ~34% of the discharge). Within the confluence zone, the main secondary cell effectively moves to the channel center between sections B4 and B5, thus forcing a certain proportion of the discharge near the bed to be deflected toward the left bank (see the direction of the corresponding primary velocity vectors in Figure 6). The bed topography along the scour hole in this zone would also contribute to this influence by topographically forcing the flow through the scour [*Lane et al.*, 2000], thus helping to maintain the secondary circulation generated upstream (CB1) through this zone. Thus the geometry of confluence B would seem to favor the maintenance of the secondary cell on the left side of the channel within the zone of flow recovery, and this further facilitates flow mixing. In confluence A, however, the extent of the scour hole is smaller and flow from the right branch essentially remains on the right hand side of the channel at section A4.

3.4. Suspended Sand Concentration, Flow Velocity, and Bed Shear Stress

[29] The total transport of suspended sand at each cross-section at the two confluences (Table 5) shows that the mean values of total suspended sediment flux (*Gss*) obtained with the aDp are of the same order to those predicted by the available suspended sand rating curve in the Río Paraná [*Alarcón et al.*, 2003], for similar discharge and bed sediment texture conditions (302.0 kg s^{-1} and 283.6 kg s^{-1} for confluences A and B respectively). Table 5 also shows that the differences between the *Gss* values at each individual cross-section compare well with the mean sand transport rates for all the sections. These estimates vary by less than ~20%, which is a satisfactory deviation for estimation of sediment transport in rivers, and provides confidence in use of the aDp to measure *Gss* and suspended sediment distributions through the sections.

[30] The suspended sand concentration fields, together with the secondary velocity fields, at each individual section at both confluences are shown in Figure 8, while the distributions of vertically-averaged primary velocity, suspended sand concentrations, and bed shear stresses across each of the sections are shown in Figure 9. At confluence A, the distribution of suspended sand in the upstream channels shows that in section A1 there is a core of higher concentration at the center of the channel, that can be related to a zone of fluid upwelling (Figure 7), while in section A2 the maximum concentrations are lower and also more evenly distributed across the channel width in the near-bed region. Sediment concentrations in section A1 appear linked to the location of higher primary velocities, which are influenced by the upstream channel where the flow is more constricted than in section A1. At section A3, the major pathway for suspended bed sediment is located in the center of the channel, within the region of maximum flow velocities (Figure 5), and appears to be a continuation of the pathway from the upstream right-hand branch. The principal sediment transport pathway is located toward the thalweg, but on the flank of the bar that extends from the upstream junction corner, and separates the region of high sediment concentrations from the area of bed scour. This region of high sediment transport is also located on the right hand side of the mixing layer (A3 at ~400 m across the section), and thus it appears that the principal sediment transport pathways are at the edge of the mixing layer and scour, and are often correlated well with positive vertical velocity (Figure 7). On the left side of section A3, slightly higher concentrations of suspended sediment are present near the bed and in the shallower regions over the bar downstream of the junction corner. However, it is evident that the left branch, at this flow stage, has a lower contribution to the total suspended sediment flux (Figure 9). The core of higher suspended sand concentration toward the middle of the channel is maintained downstream in sections A4 and A5, and is located in the regions of higher flow velocity (Figure 5) and positive vertical velocity (Figure 7). The core of suspended bed sediment transport at confluence A thus appears dominated by the sediment transport pathway from the true right channel, whose downstream translation in the

Table 5. Suspended Sand Transport Within Confluences A and B

	Suspended Sand Transport, Gss (kg s^{-1})[a]		Differences With the Mean Value (%)	
Section	San Martin Confluence (A)	Rosario Confluence (B)		
1	292.0	228.4	−17	+11
2	36.3	79.7		
3	410.6	228.4	+13	−11
4	374.2	248.4	+6	−2
5	360.9	268.2	−2	+2
Mean value	368.5	263.2		

[a]Gss mean values have an error of ±50% according to the accuracy with which Cs is predicted from Figure 2. Note that the differences with the mean values of Gss at each section are within this error.

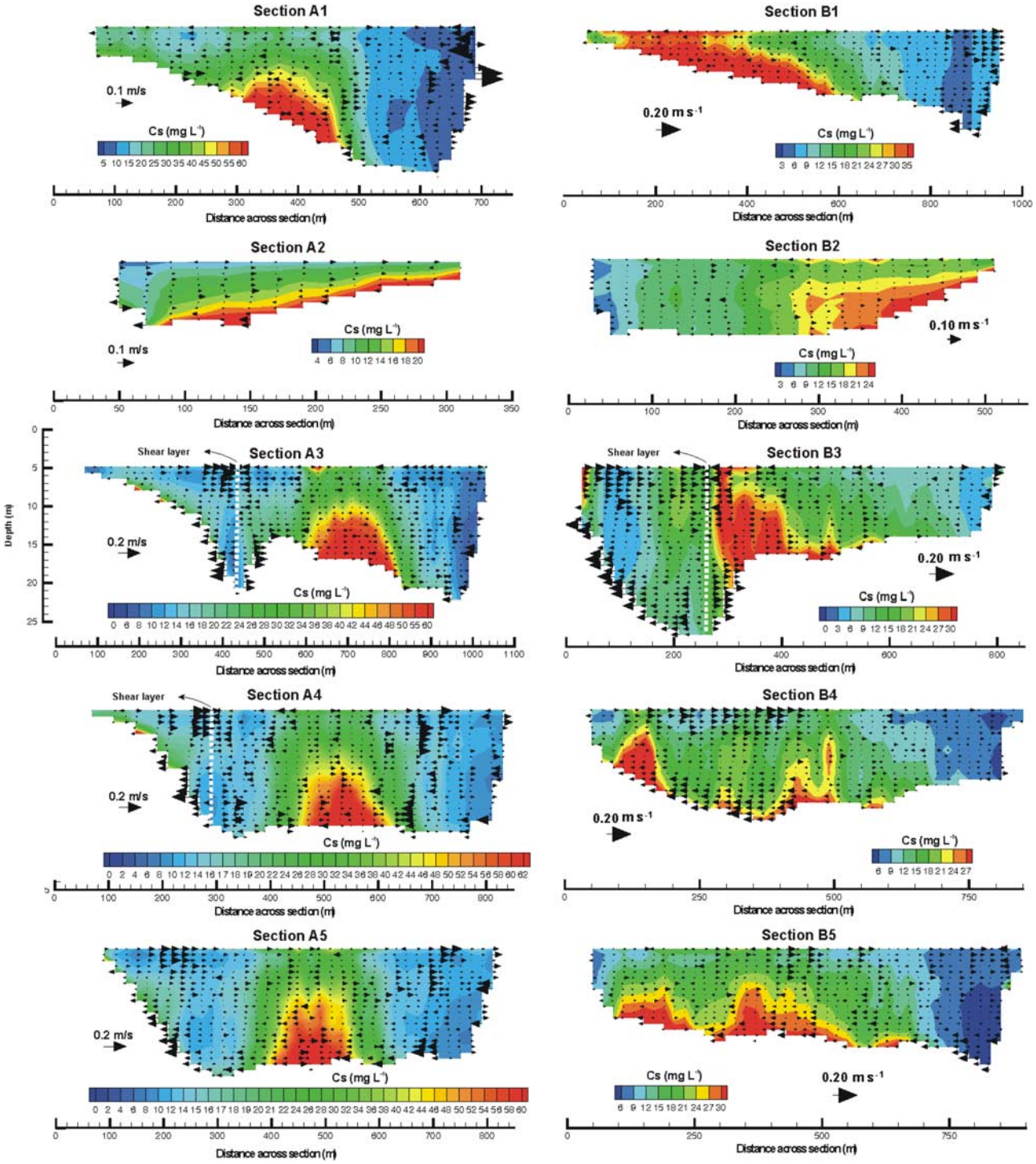

Figure 8. Suspended sand concentrations and secondary velocity fields in the surveyed sections at confluences A and B. Sections are viewed looking downstream with left bank on the left-hand side. Note: contour range and reference vector size change between plots to aid visualization. Dotted white line shows approximate position of the mixing/shear interface.

center of the post-confluence channel and on the edges of the mixing layer are the dominant characteristics.

[31] In confluence B, strongly asymmetric distributions of suspended sediment concentration are present across both incoming channels B1 and B2 (Figures 8 and 9), with the highest values in both tributaries being located in the regions near the upstream junction corner, which do not coincide with the highest flow velocities. In section B3, one principal core of high sediment transport is present, and this is located both near the edge of the morphological step at the border of the scour hole, and along the edges of the mixing layer where secondary flow cell CB2 was identified (Figure 5) and positive vertical velocities are present (Figure 7). A region of slightly higher sediment concen-

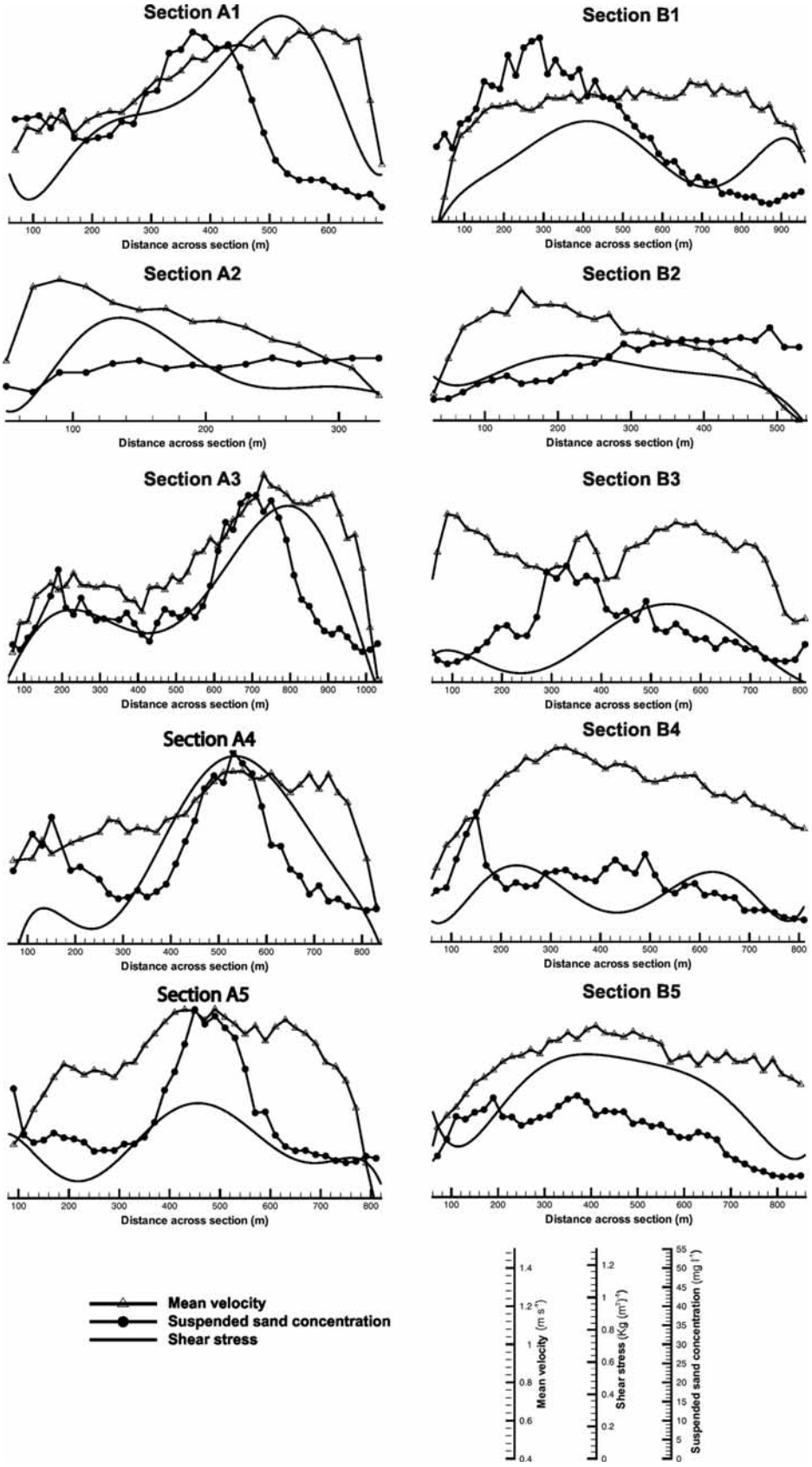

Figure 9. Mean velocity, average suspended sand concentration, and shear stress distribution across the surveyed sections at confluences A and B. Sections are viewed looking downstream with left bank on the left-hand side.

tration is also present on the left side of section B3 and may represent inertial influences on the sediment transported into the junction from the left tributary, with lower suspended sediment values recorded between this point and the left bank, despite this area coinciding with relatively higher primary flow velocities. In section B4, there are two regions of higher sediment concentration. The area at the center of the channel (at c. 425 m) is on the right downstream margin of the scour hole, and may represent the downstream continuation of the core of higher transport present at section B3: this area is both along the edge of the scour and also the edge of the mixing layer, and lies in a region of lower shear stresses (Figure 9). The second core is located at c. 125 m, again outside of the region of highest bed shear stresses, and on the margin of the bar that is present at the left bank. Although the source of these cores of higher sediment transport cannot be discerned, it may be speculated that each represents the supply of sediment from the upstream tributaries that has been routed around the edges of the scour, mixing layer and secondary cell, and are thus spatially separated at this locality. Such peaks in bed load transport rate at the edges of the junction scour have been reported from laboratory experiments [*Best*, 1988] and also more recently from the field [*Boyer et al.*, 2006]. At the downstream section B5, the two cores of high sediment transport become closer together and appear to spread across channel in a region that is at the very downstream end of the confluence scour (Figure 2). The core of higher suspended bed sediment transport in section B5 at c. 350 m is linked to maximum bed shear stresses, although the small core of sediment transport to the left has lower associated bed shear stresses.

[32] Suspended bed sediment transport at these two large confluences thus shows spatial concentration within distinct corridors, and these appear related to both the flow structure within the junction and the upstream sediment supply pathways. Confluence A is dominated by the transport of sediment from the major tributary, with sediment being transported along the edges of the mixing layer and being topographically steered by the bar from this channel that borders the scour. At this discharge ratio (0.2), it appears that the major channel is dominant in controlling the spatial distribution of suspended bed sediment, and that the minor left channel has a far smaller contribution. The regions of higher velocity and bed shear stress in the upstream right-hand channel thus dominate the input of sediment, which then forms a distinct pathway in the middle of the downstream channel. At confluence B, where the discharge ratio is higher (0.5), the right-hand channel supplies sediment into the junction where it appears to be both steered by the topography as well as being concentrated toward the edges of the mixing layer. The presence of a secondary flow cell at this location may also aid this transport pathway, and results in a clear peak in transport at section B3 that is not in a zone of the highest bed shear stress. Past work [e.g., *Boyer et al.*, 2006] has also shown both that the region of highest sediment transport may be at the edges of the mixing layer in confluences and that this region is correlated with high transverse-vertical cross stresses, rather than normal stresses. This may help explain the poor correlation between bed shear stress and transport rate reported herein. Indeed, such routing may be even more significant in larger channel confluences where channel-scale secondary currents may be too weak and/or spatially restricted to influence these cores of high sediment concentration. At the sections below the junction, two cores of high sediment transport occur and may represent the routing of sediment from each tributary around the scour (topographic forcing) and high transport rates at the edges of the mixing layer. As flow and sediment moves downstream, and the junction scour becomes shallower and wider, these two corridors of high sediment transport become less distinct as the sediment begins to mix across channel downstream, as has been reported in past laboratory studies [*Best*, 1988].

4. Discussion

[33] The data presented herein enable a first analysis of the interactions between morphology, flow structure and suspended bed sediment at two bar confluences within a large river where *W*/*D* ratios are high. Although in both confluences reported herein appreciable zones of scour exist where the two flows combine, there are notable differences between the two sites. The dimensionless scour depth equates to twice the pre-confluence average main channel depth in confluence A, compared with approximately 2.5 times in confluence B, and these values compare well with those found at smaller confluences (W < 10 m), laboratory investigations [*Ashmore and Parker*, 1983; *Best*, 1986, 1988; *Boyer et al.*, 2006] and limited work at other large channel confluences [*Best and Ashworth*, 1997; *Best et al.*, 2007; *Best and Rhoads*, 2008; *Parsons et al.*, 2008]. Additionally, similar to the findings by *Best and Ashworth* [1997] from a large confluence, both scours have very low slope angles that dip into the central scour. The bed slopes along the longitudinal streamlines between the left branches and sections A3 and B3 are both small, with angles of ~1 degree and ~1.5 degrees respectively, and far too low to generate any flow separation as often observed over the steeper morphological steps found at many smaller channel confluences [e.g., *Best*, 1988; *Best and Roy*, 1991; *Biron et al.*, 1993b; *McLelland et al.*, 1996]. This implies that spatial scale might be an important parameter controlling the presence of steeper scour faces and thus impart a significant control on flow structure, mixing and sedimentology [*Parsons et al.*, 2008].

[34] The positions of the scour holes in both confluences A and B appears dependent on the flow momentum ratio between the two confluent channels, i.e. between mid-channel and right bank if $Q_L/Q_R > 1$ and nearer the left bank if $Q_L/Q_R < 1$, supporting previous field and experimental results in smaller junctions [*Mosley*, 1976; *Best*, 1987, 1988]. However, in these larger channels the discharge ratio, Q_L/Q_R, may not be the most important variable controlling the position and dimensions of the scour hole: the location and distribution of the cores of primary velocity across the widths of the confluent channels may have the most significant influence, particularly where the high *W*/*D* ratios allow for a greater variability in this distribution. In confluence B, for example, the main core of flow is closer to the true right bank, producing a large asymmetry in the spanwise distribution of flow at the confluence. The possibility of such asymmetry in primary flow velocity may tend to increase in large rivers, where *W*/*D* ratios are larger, and

thus may exert a previously unrecognized influence on the flow dynamics of confluences at larger spatial scales. The difference in the position of scour between the two confluences is therefore likely influenced by differences in the degree of width constriction. This constriction is notably higher in confluence B, which results in flow acceleration between the mixing interface and the left bank at section B3. In confluence A, however, despite a lower overall momentum ratio (Table 1), flow from the left branch channel is not constricted and accelerated as much as the flows combine as in confluence B.

[35] Analysis of flow at both confluences highlights the importance of the distribution of velocity within the incoming channels in driving flow mixing and the distribution of suspended sand, although it is clear that the normal bed shear stresses may not be the primary factor promoting such sediment suspension. Zones of secondary circulation are identified in both confluences and form cells close to the zones of flow shear/mixing above the scours, and resemble those found in smaller confluences [e.g., *Mosley*, 1976; *Ashmore et al.*, 1992; *Rhoads*, 1996]. However, these secondary cells cover less than ~20 % of the channel width, unlike those measured at smaller confluences where these cells may extend up to 50–80% of the channel width [*Rhoads and Kenworthy*, 1995; *Rhoads and Sukhodolov*, 2001].

[36] The analysis above can be used to unravel the mechanisms producing the secondary flows observed within these large confluences and provides explanations for a number of their properties, including their limited spatial extent and attenuation as these secondary cells are advected downstream. The reduction in magnitude of primary velocity within the shear layer (Figure 5) generates a notable transverse velocity gradient in both confluences (sections A3 and B3). Such a reduction of velocity, together with motion originating due to the transverse shear, results in a transfer of energy from the mean flow to turbulence in the generation of large-scale, two-dimensional turbulent structures. These velocity gradients diminish through sections A4 and B4, and are accompanied by a diminution of the secondary circulation cells. The presence of large-scale dunes in the Río Paraná [e.g., *Amsler and Schreider*, 1999; *Amsler and Prendes*, 2000; *Parsons et al.*, 2007], with dune heights of up to 3.5 m through the study reach under similar hydraulic conditions to the measurements presented herein [e.g., *Amsler and Prendes*, 2000], would also impart considerable form roughness to the flow. Such form roughness could lead to the merging of the two cores of primary velocity, thereby reducing the transverse velocity gradient and resulting in the decline of coherent, channel-scale, secondary flow [e.g., *Parsons et al.*, 2007].

[37] Previous studies reporting on smaller confluences have argued that the pattern of secondary flow cells formed at junctions can result from flow curvature and the associated interaction between centrifugal acceleration and pressure gradients through the confluence zone [*Rhoads*, 1996; *Rhoads and Kenworthy*, 1998; *Rhoads and Sukhodolov*, 2001]. The centrifugal effect within an asymmetrical confluence produces superelevation of the water surface along the mixing interface near the junction apex as well as along the center of the main channel. This centrifugal force varies through the flow depth, resulting in a net pressure gradient force that generates a return flow at the bed from the central confluence scour toward the channel banks [e.g., *Rhoads and Kenworthy*, 1998; *Bradbrook et al.*, 2000]. The result is a flow mechanism that resembles the well-known model proposed to explain helical flow within a meander bend, with flow in the central region of small asymmetrical confluences generating twin, ''back-to-back,'' counter-rotating helical flow cells [*Mosley*, 1976; *Best*, 1986; *Rhoads and Kenworthy*, 1998; *Bradbrook et al.*, 2000]. Other investigators have also linked the existence of secondary flow cells to both the deformation and interactions of the shear layer [*Best and Roy*, 1991; *Lane et al.*, 2000], and to flow separation in the lee side of avalanche faces that may dip into the scour [e.g., *Best*, 1986, 1988; *Best and Roy*, 1991; *Biron et al.*, 1993b]. Using the expression $\Delta E = (V^2 W/(gr))$, as suggested by *Dietrich* [1987] for river bends, it is possible to estimate the total water surface elevation, ΔE, due to centrifugal effects in these confluences (where V is the cross-sectional average downstream mean velocity; W is the flow width; g is the gravitational acceleration and r is the local radius of curvature of the centerline). For instance, if this expression is applied to the left branch flow in section B3, with $V \approx 1.5$ m s^{-1}, $W \approx 250$ m and $r \approx 1900$ m, the resulting superelevation, ΔE is $\approx 0.02–0.03$ m. Although this is relatively low given the width of the channel, it is similar in magnitude to the streamwise water surface slope of the reach. However, in such an analysis, the shear layer is assumed to be a solid boundary, whereas in reality it is ''permeable'' due to shear layer deformation and mixing along the interface between the two converging flows, and thus the actual value of superelevation may be considerably lower. Additionally, the influence of the confluence scour zone upon the extent over which the pressure gradient overcomes any influence of form roughness must also be considered. Although the scour slopes in confluences A and B would not produce flow separation, the generation of pressure gradients due to discordance or scour can be strong enough to trigger secondary circulation, even in the absence of flow separation. Given this, the secondary circulation patterns produced within these two large confluences are likely to result from the shear between the two flows as they combine over the zone of scour, similar to the mechanism described by *Lane et al.* [2000]. Beyond this zone of scour, the influence of declining shear gradients away from the mixing interface, combined with the pressure gradients across the scour edges, means that in these channels the forces acting to produce secondary circulation are too small to overcome form roughness [*Parsons et al.*, 2007]. This acts to restrict the secondary circulation to small portions of the channel width, in the deeper regions of scour close to the shear interface, as highlighted by the patterns of vertical velocity (Figure 7). Such topographic restriction of the extent of secondary flow cells has been highlighted for meander bends by *Dietrich and Smith* [1983], where flow is topographically forced across point bars that restrict the pressure gradient effects and reduce the effective width of the cells.

[38] The distributions of suspended sediment concentration through the two confluences also qualitatively correspond with measurements performed at asymmetric junctions in laboratory channels and recent work in small confluences. Qualitative [*Mosley*, 1975, 1976] as well as

quantitative [*Best*, 1988] observations suggest that the largest sediment transport pathways occur essentially surrounding the scour hole, and this, together with the high turbulence levels along the shear layer, act to maintain the scour [*Boyer et al.*, 2006]. Figures 8 and 9 (section A3 and B3) show this same tendency in sediment transport at this larger scale, albeit modified by the non-uniform distributions of transport in the upstream sections, with the highest concentrations of suspended bed sediment being along the flank of the scour within both confluences.

5. Conclusions

[39] The present paper provides a description and comparison of the principal characteristics of the morphology, flow structure and suspended sediment transport of two large, asymmetrical, bar-confluence units in the Río Paraná, Argentina. Major findings include:

[40] 1. A number of features similar to those reported from far smaller confluences, with lower *W*/*D* ratios, were recorded. These include shear or mixing layers where the two flows combine; zones of secondary circulation, albeit restricted to narrow proportions of the total channel width, and a region of progressive flow recovery downstream from the confluence.

[41] 2. The position of the scour hole appears dependent on the flow momentum ratio between the two confluent rivers, supporting previous field and experimental results in small junctions [*Mosley*, 1976; *Best*, 1987, 1988]. However, the discharge ratio Q_L/Q_R may not be the most important variable controlling the position and dimensions of the scour hole, since the actual location and distribution of the cores of primary velocity across the large widths of the confluent channels may have the most significant influence. The possibility of a large asymmetry in the spanwise distribution of primary flow velocity may tend to increase in large rivers, where *W*/*D* ratios are generally much larger [*Xu*, 2004], and thus may exert a previously unrecognized influence on the flow dynamics of confluences with increasing spatial scale. Thus an approach that assesses the "local" momentum ratio between the cores of high velocity fluid, rather than the momentum ratio across the entire channel width, may be a better predictor of confluence morphology in *s*uch wide channels. Future study of, and comparison with, smaller channels with a similar *W*/*D* ratio to the channels reported herein, may further elucidate whether it is the absolute channel scale or *W*/*D* ratio that is the predominant control on this velocity asymmetry.

[42] 3. Bed discordance between the confluent branches is present at both junctions but they do not form true "avalanche faces." The flanks of the scours are very low angle and are incapable of generating regions of permanent flow separation as observed at many smaller confluences with lower *W*/*D* ratios.

[43] 4. Secondary circulation, although present, is restricted to less than ~20 % of the channel width, unlike those cells measured at smaller confluences where the width of such cells may extend up to 50–80 % of the channel width. Moreover, this restriction of secondary circulation seems related to the generative mechanisms of secondary flows at these higher *W*/*D* ratios, which are found to be dominated by shear-induced turbulence and concentrated close to the mixing interface over the scour region. The secondary cells that form at these large junctions are topographically controlled into narrow portions of the channel width.

[44] 5. Finally, the distribution of suspended bed sediment within these confluences is found to be dependent on the sediment distributions across the upstream confluent channels, with the corridors of greatest sediment transport occurring around the flanks of the scour hole. Such patterns have also been revealed in laboratory studies of asymmetric junctions and small channel confluences, and may play a key role in the generation and maintenance of confluence scour across spatial scales.

[45] There is a clear need for further field study, combined with detailed modeling investigations, to examine how the findings and results identified and discussed in this paper can be generalized and assess the nature of scale invariance in the operation of these processes at these key sites in fluvial networks.

Notation

The following symbols are used in this paper:

- a regression slope coefficient.
- AI aDp averaging interval, seconds.
- b regression intercept coefficient.
- CS aDp cell size, m.
- d distance from the aDp transducer, m.
- D depth, m.
- EL signal intensity as reported by the aDp.
- g gravitational acceleration, ms^{-2}.
- Gss suspended sand transport at given cross section, $kg\ s^{-1}$.
- M flow momentum ratio = $(\rho Q_L V_L)/(\rho Q_R V_R)$
- PL length of the acoustic pulse.
- pr particle radius, μm.
- Q total discharge, m^3s^{-1}.
- Q_L left branch discharge, m^3s^{-1}.
- Q_R right branch discharge, m^3s^{-1}.
- r local radius of curvature of the centerline, m.
- R distance between the transducer and the measurement volume, m.
- RS relationship between pressure at transducer face and measured signal strength.
- SL measure of the transmitted acoustic power.
- Sv volume scattering strength, dB.
- U_* bed shear velocity, $m\ s^{-1}$.
- v point velocity, $m\ s^{-1}$.
- v_N northerly component of the point velocity vector, $m\ s^{-1}$.
- v_E eastward component of the point velocity vector, $m\ s^{-1}$.
- v_P point primary velocity, $m\ s^{-1}$.
- v_S point secondary velocity, $m\ s^{-1}$.
- V cross section average velocity, $m\ s^{-1}$.
- V_L cross section average velocity (left branches), $m\ s^{-1}$.
- V_R cross section average velocity (right branches), $m\ s^{-1}$.
- W width, m.
- W_A post-confluence mean channel width of confluence A, m.
- W_B post-confluence mean channel width of confluence B, m.
- z height above bed, m.

x position coordinate, m.
y position coordinate, m.
θ orientation of v with respect to north, degrees.
α orientation with respect to north for the depth average velocity vector, degrees.
ρ water density, kg m^{-3}.
ΔE total water surface elevation, m.
κ von Karman constant ($\sim$0.4).
τ bed shear stress, kg m^{-2}
α_s sound absorption coefficient, dB m^{-1}.
α_L angle of deviation between the left branches relative to the downstream channel
α_R angle of deviation between the right branches relative to the downstream channel

[46] **Acknowledgments.** The authors are grateful for the field surveys conducted by Eng. Jose Huespe, who is responsible for the hydrographic measurements conducted at FICH. This study was made within the framework of the project "Morphology and Hydraulic Features of Nodal Points in the Río Paraná main Channel" granted by the Universidad Nacional del Litoral of Santa Fe, Argentina. RNS thanks the Earth and Biosphere Institute at the University of Leeds for funding a 4-month research fellowship, which enabled the writing of this paper. JLB and DRP thank the UK Natural Environment Research Council for funding through grants NER/A/S/2001/00445 and NER/B/S/2003/00243 and the UK Royal Society for a Joint International Project. DRP also thanks NERC for his Fellowship funding in grant NE/C002636/1. We are extremely grateful for the constructive comments of the two referees and associate editor that have helped to greatly improve the paper.

References

Alarcón, J., R. Szupiany, M. Montagnini, H. Gaudin, H. Prendes, and M. Amsler (2003), *Evaluación del Transporte de Sedimentos en el Tramo Medio del Río Paraná*, Hidráulica de Ríos, Buenos Aires, Argentina.

Amsler, M. L., and M. I. Schreider (1999), Dune height prediction at floods in the Paraná River, Argentina, in *River Sedimentation*, edited by A. W. Jayawardena et al., pp. 615–620, A. A. Balkema, Brookfield, Vt.

Amsler, M. L., and H. H. Prendes (2000), Transporte de Sedimentos y Procesos Fluviales Asociados, in *El Río Paraná en su Tramo Medio*, edited by C. Paoli and M. Scheirder, pp. 312, Centro de Publicaciones, Universidad Nacional del Litoral, Santa Fe, Argentina.

Ashmore, P. E., and G. Parker (1983), Confluence scour in coarse braided streams, *Water Resour. Res.*, *19*, 392–402.

Ashmore, P. E., R. L. Ferguson, K. L. Prestegaard, P. J. Ashworth, and C. Paola (1992), Secondary flow in anabranch confluences of a braided, gravel-bed stream, *Earth Surf. Processes Landforms*, *17*, 299–311.

Ashworth, P. J., J. L. Best, J. Roden, C. S. Bristow, and G. J. Klaassen (2000), Morphological evolution and dynamics of a large, sand braid-bar, Jamuna River, Bangladesh, *Sedimentology*, *47*, 533–555.

Best, J. L. (1986), The morphology of river channel confluences, *Prog. Phys. Geogr.*, *10*, 157–174.

Best, J. L. (1987), Flow dynamics at river channel confluences: Implications for sediment transport and bed morphology, in *Recent Developments in Fluvial Sedimentology*, edited by F. G. Ethridge et al., pp. 27–35, Soc. of Econ. Paleontol. and Mineral., Tulsa, Okla.

Best, J. L. (1988), Sediment transport and bed morphology at river channel confluences, *Sedimentology*, *35*, 481–498.

Best, J. L., and P. Ashworth (1997), Scour in large braided rivers and the recognition of sequence stratigraphic boundaries, *Nature*, *387*, 275–277.

Best, J. L., and B. L. Rhoads (2008), Sediment transport, bed morphology and the sedimentology of river channel confluences, in *River Confluences, Tributaries and the Fluvial Network*, edited by S. P. Rice, A. Roy, and B. L. Rhoads, pp. 45–72, Wiley-Interscience, Hoboken, N. J.

Best, J. L., and A. G. Roy (1991), Mixing-layer distortion at the confluence of channels of different depth, *Nature*, *350*(6317), 411–413.

Best, J., P. Ashworth, M. H. Sarker, and R. Roden (2007), The Brahmaputra-Jamuna River, Bangladesh, in *Large Rivers: Geomorphology & Management*, edited by A. Gupta, pp. 395–430, John Wiley, Holboken, N. J.

Biron, P. M., and S. N. Lane (2008), Modelling hydraulics and sediment transport at river confluences, in *River Confluences, Tributaries and the Fluvial Network*, edited by S. P. Rice, A. Roy, and B. L. Rhoads, pp. 17–43, Wiley-Interscience, Hoboken, N. J.

Biron, P., B. De Serres, A. G. Roy, and J. L. Best (1993a), Shear layer turbulence at an unequal depth channel confluence, in *Turbulence: Perspectives on Flow and Sediment transport*, edited by N. J. Clifford et al., pp. 197–213, Wiley-Interscience, Hoboken, N. J.

Biron, P., A. G. Roy, J. L. Best, and C. J. Boyer (1993b), Bed morphology and sedimentology at the confluence of unequal depth channels, *Geomorphology*, *8*, 115–129.

Biron, P., J. L. Best, and A. G. Roy (1996a), Effects of bed discordance on flow dynamics at river channel confluences, *J. Hydraul. Eng., ASCE*, *122*(12), 676–682.

Biron, P., A. G. Roy, and J. L. Best (1996b), Turbulent flow structure at concordant and discordant open-channel confluences, *Exp. Fluids*, *21*, 437–446.

Biron, P. M., A. Richer, A. D. Kirkbride, A. G. Roy, and S. Han (2002), Spatial patterns of water surface topography at a river confluence, *Earth Surf. Processes Landforms*, *27*, 913–928.

Boyer, C., A. G. Roy, and J. L. Best (2006), Dynamics of a river channel confluence with discordant beds: Flow turbulence, bed load sediment transport, and bed morphology, *J. Geophys. Res.*, *111*, F04007, doi:10.1029/2005JF000458.

Bradbrook, K. F., S. N. Lane, and K. S. Richards (2000), Numerical simulation of three-dimensional, time-averaged flow structure at river channel confluences, *Water Resour. Res.*, *36*, 2731–2746.

Bradbrook, K. F., S. N. Lane, K. S. Richards, P. M. Biron, and A. G. Roy (2001), Role of bed discordance at asymmetrical river confluences, *J. Hydraul. Eng.*, *127*, 351–368, May.

Creed, E. L., A. M. Pence, and K. L. Rankin (2001), Inter-Comparison of Turbidity and Sediment Concentration Measurement from an ADP, an ABS-3, and a LISST, in *Oceans 2001 MTS/IEEE Conference Proceedings*, vol. 3, pp. 1750–1754, Honolulu, Hawaii.

De Serres, B., A. G. Roy, P. M. Biron, and J. L. Best (1999), Three-dimensional structure of flow at a confluence of river channel with discordant beds, *Geomorphology*, *26*, 313–335.

Drago, E., and M. L. Amsler (1988), Suspended sediment at a cross section of the Middle Paraná River: Concentration, granulometry and influence of the main tributaries, in *Sediment Budget, Proceedings of the Porto Alegre Symposium*, IAHS, Porto Alegre, Brasil, pp. 381–396.

Drago, E., and M. L. Amsler (1998), Bed sediment characteristics in the Paraná and Paraguay rivers, *Water Int.*, *23*, 174–183.

Dietrich, W. E. (1987), Mechanics of flow and sediment transport in river bends, in *River Channels: Environment and Process, Institute of British Geographers Special Publication No. 18*, edited by K. S. Richards, pp. 179–227, Basil Blackwell, Inc.

Dietrich, W. E., and J. D. Smith (1983), Influence of the point bar on flow through curved channels, *Water Resour. Res.*, *19*(5), 1173–1192.

FCEIA-UNR (Facultad de Ciencias Exactas) (1990), Estudios del tramo km. 410–440 de la ruta de navegación del río Paraná, in *Dirección Nacional de Vías Navegables*, 120 pp., Univ. Nacional de Rosario, Rosario, Argentina.

Facultad de Ingeniería y Ciencias Hídricas (FICH) (2006), Estudios complementarios hidráulicos y morfológicos de la zona de la isla de La Invernada, in *Secretaria de Puertos y Vías Navegables, Capitulo 3: Estudios de la Evolución Morfológica del Río*, 90 pp., Univ. Nacional del Litoral, Santa Fe, Argentina.

Filizola, N., and J. L. Guyot (2004), The use of Doppler technology for suspended sediment discharge determination in the River Amazon, *Hydrol. Sci. J.*, *49*, 143–153.

Klassen, G. J., and K. Vermeer (1988), Confluence scour in a large braided rivers with fine bed material, in *Proc. International Conference on Fluvial Hydraulics*, Budapest, Hungary, pp. 395–408.

Kostaschuk, R., P. Villard, and J. Best (2004), Measuring velocity and shear stress over dunes with acoustic Doppler profiler, *J. Hydraul Eng. ASCE*, *130*, 932–936.

Kostaschuk, R., J. Best, P. Villard, J. Peakall, and M. Franklin (2005), Measurement of flow velocity and sediment transport with an acoustic Doppler current profiler, *Geomorphology*, *68*, 25–37.

Lane, S. N., K. F. Bradbrook, K. F. Richards, P. M. Biron, and A. G. Roy (1999), Time-averaged flow structure in the central region of a stream confluence: A discussion, *Earth Surf. Processes Landforms*, *24*, 361–367.

Lane, S. N., K. F. Bradbrook, K. F. Richards, P. M. Biron, and A. G. Roy (2000), Secondary circulation cells in river channel confluence: Measurement artefacts or coherent flow structures?, *Hydrol. Processes*, *14*, 2047–2071.

Lane, S. N., D. R. Parsons, J. L. Best, O. Orfeo, R. Kostachuk, and R. J. Hardy (2008), Causes of rapid mixing at a junction of two large rivers: Río Paraná and Río Paraguay, Argentina, *J. Geophys. Res.*, *113*, F02024, doi:10.1029/2006JF000745.

McLelland, S. J., P. J. Ashworth, and J. L. Best (1996), The origin and downstream development of coherent flow structures at channel junctions, in *Coherent Flow Structures in Open Channels*, edited by P. J. Ashworth et al., pp. 491–519, Wiley-Interscience, Hoboken, N. J.

McLelland, S. J., P. J. Ashworth, J. L. Best, J. Roden, and G. J. Klaassen (1999), Flow structure and spatial distribution of suspended sediment around an evolving braid bar, Jamuna River, Bangladesh, in *Fluvial Sedimentology VI*, edited by N. D. Smith and J. Rogers, pp. 43–57, Spec. Publ. of Int. Assoc. of Sedimentol., Blackwell Sci., Wiley-Blackwell, London.

Mosley, M. P. (1975), An experimental study of channel confluences, Ph.D. thesis, 216 pp., Colorado State Univ., Fort Collins, Colo.

Mosley, M. P. (1976), An experimental study of channel confluences, *J. Geol.*, *84*, 535–562.

Mosley, M. P. (1982), Scour depths in branch channel confluences: Ohau River, Otago, New Zealand, Proceedings of New Zealand Institute of Professional Engineers, Otago, New Zealand.

Parsons, D. R., J. L. Best, S. N. Lane, O. Orfeo, R. J. Hardy, and R. Kostaschuk (2007), Form roughness and the absence of secondary flow in a large confluence-diffluence, Río Paraná, Argentina, *Earth Surf. Processes Landforms*, *32*, 155–162, doi:10.1002/esp.1457.

Parsons, D. R., J. L. Best, S. N. Lane, R. A. Kostaschuk, R. J. Hardy, O. Orfeo, M. L. Amsler, and R. N. Szupiany (2008), Large confluences, in *River Confluences, Tributaries and the Fluvial Network*, edited by P. Stephen Rice et al., 416 pp., John Wiley, Hoboken, N. J.

Ramonell, C. G., M. L. Amsler, and H. Toniolo (2002), Shifting modes of the Paraná River thalweg in its middle/lower reach, *Zeitschr. Geomorphol.*, *129*, 129–142.

Reid, I., J. L. Best, and L. E. Frostick (1989), Floods and flood sediments at river confluences, in *Floods: Hydrological, Sedimentological and Geomorphological Implications*, edited by K. Beven and P. A. Carling, pp. 135–150, Wiley-Interscience, Hoboken, N. J.

Rhoads, B. L. (1996), Mean structure of transport-effective flows at an asymmetrical confluence when the main stream is dominant, in *Coherent Flows Structure in Open Channel*, edited by P. J. Ashworth et al., pp. 491–517, Wiley-Interscience, Hoboken, N. J.

Rhoads, B. L., and S. T. Kenworthy (1995), Flow structure in asymmetrical stream confluence, *Geomorphology*, *11*, 273–293.

Rhoads, B. L., and S. T. Kenworthy (1998), Time-average flow structure in the central region of a stream confluence, *Earth Surf. Processes Landforms*, *23*, 171–191.

Rhoads, B. L., and S. T. Kenworthy (1999), On secondary circulation, helical motion and Rozovskii-based analysis of time-averaged two-dimensional velocity fields at confluence, *Earth Surf. Processes Landforms*, *24*, 369–375.

Rhoads, B. L., and A. N. Sukhodolov (2001), Field investigation of three-dimensional flow structure at stream confluences: 1. Thermal mixing and time-averaged velocities, *Water Resour. Res.*, *37*, 2393–2410.

Richardson, W. R., C. R. Thorne, and S. Mahmood (1996), Secondary flow and channel changes around a bar in the Brahmaputra River, Bangladesh, in *Coherent Flow Structures in Open Channel*, edited by P. J. Ashworth et al., pp. 519–545, Wiley-Interscience, Hoboken, N. J.

Richardson, W. R., and C. R. Thorne (1998), Secondary Currents around a Braid Bar in the Brahmaputra River, Bangladesh, *J. Hydraul. Eng.*, *124*(3), 325–328.

Richardson, W. R., and C. R. Thorne (2001), Multiple thread flow and channel bifurcation in a braided river: Brahmaputra-Jamuna River, Bangladesh, *Geomorphology*, *38*, 185–196.

Sambrook Smith, G., P. J. Ashworth, J. L. Best, J. Woodward, and C. J. Simpson (2005), The morphology and facies of sandy braided rivers: Some considerations of scale invariance, in *Fluvial Sedimentology VII*, edited by M. Blum et al., pp. 145–158, IAS Spec. Publ. 35, Blackwell, Malden, Mass.

Schumm, S. A., and B. R. Winkley (1994), The character of large alluvial rivers, in *The Variability of Large Alluvial Rivers*, edited by S. A. Schumm and B. R. Winkley, 467 pp., ASCE, New York.

SERMAN y Asociados, S. A. (1998), Estudio hidráulico del puente principal y viaducto este, Informe Conexión Física Rosario-Victoria, G/G/ME/201, in *Convenio Gob. Nacional - Prov. de Santa Fe y Entre Ríos*, Puentes del Litoral S.A., Santa Fe, Argentina.

Sontek (1997), *Sontek Doppler Current Meters - Using Signal Strength Data to Monitor Suspended Sediment Concentration*, Sontek Application Note, San Diego, Calif.

Sontek (2000), *ADP Acoustic Doppler Profiler*, technical documentation, 143 pp., San Diego, Calif.

Szupiany, R. N., M. L. Amsler, J. L. Best, and D. R. Parsons (2007), Comparison of fixed- and moving vessel measurements with an aDp in a large river, *J. Hydraul. Eng.*, *133*(12), 1299–1310.

Xu, J. (2004), Comparison of hydraulic geometry between sand- and gravel-bed rivers in relation to channel pattern discrimination, *Earth Surf. Processes Landforms*, *29*, 645–657.

M. L. Amsler and R. N. Szupiany, National Council of Scientific and Technical Researches (CONICET), International Center for Large River Research (CIEGRI), Faculty of Engineering and Water Sciences, Littoral National University, Santa Fe City, Santa Fe, CP 3000, CC 217, Argentina.

J. L. Best, Departments of Geology and Geography and Ven Te Chow Hydrosystems Laboratory, University of Illinois, Green Street, Urbana, IL 61801, USA.

D. R. Parsons, School of Earth and Environment, Earth and Biosphere Institute, University of Leeds, Woodhouse Lane, Leeds LS2 9JT, UK. (d.parsons@see.leeds.ac.uk)